Development and Testing of Slug Calorimeter and Total Pressure Probes for a Miniaturized Arc-jet

Omar Valeinis *, Eric Won Keun Chang†, and Tobias A. Hermann‡
University of Oxford, Southwell Building , Osney Mead, OX2 0ES Oxford, United Kingdom.

This work presents designs for a set of calibration instrumentation, developed for use with a new thermal arc-jet plasma generator. This instrumentation will be used to determine the mass-specific stagnation-point enthalpy of the plasma flow, allowing for calibration of the facility to a desired set point. The stagnation-point cold-wall heat flux rate is characterized using a slug calorimeter, featuring a pair of ceramic insulators to minimize heat losses from the slug. Thermal simulations indicate acceptably low slug heat losses and high measurement accuracy, based upon a predicted stagnation-point enthalpy of 15 MJ/kg. The thermal stresses in the device indicate that an exposure time of 2s can be achieved without damaging the device. The design for a total pressure probe is also presented, with accompanying numerical analyses indicating that high exposure times are achievable, with a response time of approximately 3ms. Preliminary experimental data from calorimeter measurements indicate a stagnation-point heat flux rate of 0.85 MW/m^2, at the highest tested arc current of 80 A.

I. Nomenclature

Latin Letters

A	=	Frontal area of slug	A_i	=	Throat area
a	=	Speed of sound	c_p	=	Constant-pressure specific heat capacity
D_1	=	Parameter in Eq. (9)	D_2	=	Parameter in Eq. (9)
d	=	Slug diameter	E	=	Elastic modulus
h	=	Mass-specific enthalpy	I	=	Parameter in Eq. (13)
K_{conv}	=	Stagnation-point heat transfer coefficient	K_i	=	Argon gas property
k	=	Thermal conductivity	L	=	Slug length
l	=	Length of internal channel	M	=	Mach number
m	=	Slug mass	$\dot{m}$	=	Plasma mass flowrate
n	=	Number of mesh elements	P	=	Pressure
q	=	Surface heat flux rate	$\bar{q}$	=	Average surface heat flux rate
R	=	Specific gas constant	R_2	=	Coefficient of determination
r	=	Radius of curvature	T	=	Temperature
t	=	Time	u	=	Flow velocity
V	=	Volume of internal channel	x	=	Distance from stagnation point

Greek Letters

α	=	Linear thermal expansion coefficient	γ	=	Heat capacity ratio
θ	=	Angle from stagnation point	θ_0	=	Angle subtended by front face of slug
ν	=	Poisson ratio	ρ	=	Mass density
σ	=	Stress	τ	=	Time in Eq. (5)

*Masters Student, University of Oxford
†Postdoctoral Research Assistant, University of Oxford, Oxford Thermofluids Institute, United Kingdom.
‡Departmental Lecturer, University of Oxford, Oxford Thermofluids Institute, United Kingdom

Subscripts and Superscripts

$*$	=	Value at throat	∞	=	Free-stream value
0	=	Stagnation-point value	1	=	Time at which flow is switched on
2	=	Time at which flow is switched off	99	=	99% rise time
av	=	Volume average value	c	=	Compressive strength
I	=	First principal stress	II	=	Second principal stress
III	=	Third principal stress	m	=	Melting temperature
p	=	Pressure wave propagation time	r	=	Pressure probe response time
t	=	Tensile strength	v	=	Value within vacuum chamber
vm	=	Von Mises stress	w	=	Value at free surface
y	=	Yield stress			

II. Introduction

Plasma facilities are a type of facility used in the aerothermodynamic research of thermal protection systems. These facilities produce continuous, high-enthalpy flows, which are representative of the flow fields generated by spacecraft entering the atmosphere of a planet. At the University of Oxford, the new Osney Plasma Generator 1 (OPG1) test facility has recently been commissioned. OPG1 is a thermal arc-jet plasma generator based around a Tungsten Inter Gas (TIG) welding power supply, capable of generating currents of up to 500 A, with powers of up to 21.5 kW [1, 2]. Argon gas is passed through an electric arc and is heated up to temperatures where a plasma is formed – this is then expanded through a nozzle, with the produced jet impinging on a material test sample located in a vacuum chamber. By controlling the supply current, and the mass flow rate of argon through the nozzle, the properties of the flow can be adjusted to match realistic re-entry scenarios with accurate sensing devices required to characterize the flow field.

Kolesnikov suggests that in order to ensure local similarity with flight conditions, the key scaling parameters of mass-specific enthalpy, velocity gradient and total pressure must be carefully controlled [3], based upon the seminal work of Fay and Riddell [4]. In this work, the main flow parameter of concern is the plasma mass-specific stagnation enthalpy h_0, which must be equal to that of the entry scenario being replicated. This can be calculated from the stagnation-point pressure P_0 and stagnation-point heat flux q_0 as follows [5]:

$$q_0 = h_0 K_i \sqrt{\frac{P_0}{r}}, \tag{1}$$

where r is the effective radius of the test piece, and K_i is a property of the working gas used. In many arc-jet facilities, P_0 and q_0 are measured by using a total pressure probe and calorimeter respectively, which are typically combined into a single device fulfilling both of these functions [6]. Given the small size of this facility compared to many of its contemporaries, it was decided that these instruments should be separated in order to minimize the probe geometries as much as possible. Making the measurement instrumentation smaller will reduce flow blockage, and a smaller sensing area will provide more localized measurements of the stagnation conditions. This work presents designs for a slug calorimeter and a pressure probe to characterize the free-stream plasma flow of OPG1. Four separate sizes of calorimeter, ranging from 15mm to 35mm in diameter, have been designed. The need for different sizes is motivated by the dependence of heat transfer rate upon probe radius, which means that although the smallest probes should offer the best performance, they also have the shortest available exposure times for a given test condition. Next, a design for a 35mm diameter total pressure probe is presented - here a single size is sufficient, as total pressure is independent of probe radius. Both numerical methods and experimental data will be used to assess the performance of these designs. The main performance criterion of concern is measurement accuracy, but also of concern is the expected lifetime of each instrument, as well as available exposure time. The last two of these criteria require the continuous structural integrity of both devices, which will be compromised by melting, or any mechanical failures due to thermal stress.

III. Slug calorimeter

A. Calorimetry principles

Though there are many possible approaches to designing a heat flux sensor, the conventional approach for continuous, high-enthalpy facilities are all based upon the principle of calorimetry [7]. The surface-average heat flux rate $\bar{q}$ can be

inferred from the measured rate of change of temperature over time $\frac{\partial T}{\partial t}$, according to a heat balance for the material:

$$\bar{q}A = \rho V c_p \frac{\partial T}{\partial t}, \tag{2}$$

where ρ is the material mass density, V is the volume of the sensing element and c_p is the material specific heat capacity.

Slug calorimeters measure the temperature rise of a block (slug) of metallic material over time. These devices are simple and cheap to fabricate, and can give a faster response than liquid calorimeters, without the short exposure time limitation of thin-skin calorimeters [8–10]. If the slug calorimeter can be operated without a coolant, then it is also easier to install than liquid calorimeters, as there is no need for liquid seals. The main drawbacks of slug calorimeters are the long cool-down time required after exposure, and the short lifetime of the slug due to oxidation, ablation and the risk of melting [9]. However, the lifetime of the slug can be extended by limiting the exposure time, to ensure that degradation of the slug due to melting and ablation are minimized. The use of pure argon as a test gas prevents oxidation. The long cool-down time will not be an problem with OPG1, due to the long intervals between tests required for venting and evacuating the test chamber. For these reasons, it was decided to use a slug calorimeter as the stagnation-point heat flux sensor for OPG1.

The body of the calorimeter provides structural support to the slug and its insulation, as well as defining the external geometry of the probe. These are typically designed as either flat-faced cylinders or hemispheres. Given that the heat transfer correlations for flows over hemispherical bodies are generally more well-defined than those for flat-faced cylinders [11], it was decided to design a hemispherical probe body, with a slug featuring a curved front face. While this comes with the added complication of a non-uniform heat flux at the slug's front face, this can be accounted for by noting that surface-average heat flux $\bar{q}$ shown in Eq. (2) can be related to the stagnation-point heat flux q_0, via the geometry of the slug. This is detailed in Appendix A.

B. Literature review

Although standards for the design and production of slug calorimeters have been made by the ASTM, there is still some variation in the slug calorimeters used at different plasma facilities around the world. The findings of a literature review (Refs. [12–16]) indicate that using solid ceramic components to insulate the slug from its support is a popular choice. Ceramics are used due to their low thermal conductivity and high temperature resistance relative to most other types of solid material. Therefore, it was decided that the calorimeter design for OPG1 should also use a ceramic insulator. This presents the challenges of selecting a suitable material to use for this insulator, and ensuring the overall size of the calorimeter design can be minimized while offering acceptable measurement accuracy.

Every plasma facility requires a stagnation-point heat flux measurement to calibrate, which in turn requires a calorimeter or similar device to characterize. Given that the nozzle geometry governs the diameter of the plasma jet in each case, it is important to consider these parameters when examining existing calorimeter designs. Note that it would be inappropriate to use a calorimeter designed for a large facility with a smaller facility such as OPG1. This is due to the large flow obstruction provided by a probe that is too large, along with the poor spatial resolution of measurements that would result from a slug that is too large. Therefore, although existing calorimeter designs can be investigated, and their performances evaluated for their respective facilities, the differences between facilities must also be considered when designing a calorimeter for a new facility.

C. Material selection

The materials shown in Table 1 are used during the calorimeter design process, as well as the final design. Note that MACOR™ is not used in initial numerical models. Based upon the maximum safe temperature data shown, it was decided to set a threshold of approximately 800 K as the target slug temperature within the calorimeter. This is also a suitable maximum temperature for the glass-wrapped K-type thermocouples used in the calorimeter design [17]. It is important to note that some of the physical properties of these materials are highly temperature dependent. It is generally assumed that unless a temperature dependence is pre-defined in the software used, then a material property is constant with temperature, using the values given in Table 1. One exception to this is the constant-pressure specific heat capacity c_p of oxygen-free high conductivity (OFHC) copper, which varies with average temperature T_{av} according to the Shomate equation [15]:

$$\begin{aligned} c_p(T_{av}) = {} & 2.789922 \times 10^2 + 4.421789 \times 10^{-1}\, T_{av} - 4.918152 \times 10^{-4}\, (T_{av})^2 \\ & + 2.19879 \times 10^{-7}\, (T_{av})^3 + 1.079706 \times 10^6\, (T_{av})^{-2} \end{aligned} \tag{3}$$

Brass is used to provide structural support within the calorimeter, so it is important that its mechanical behavior is well-understood. From Ref. [18], the proof stress of CW614N brass is taken to be 300 MPa at 0.2% strain. This value of strain is therefore used as the yield threshold for this material. From simulation results, it is possible to calculate a 'stress-equivalent' strain (= σ_{vm}/E), from which the real stress state of the brass can be determined. It is necessary to evaluate the material state in this manner due to limitations of the software being used, which means that the brass can only be modeled as a linear elastic material, when in reality it will exhibit highly ductile behavior in the plastic regime.

Failure in the ceramic components is modeled using the maximum principal stress failure criterion, in which fracture occurs if the tensile strength σ_t or compressive strength σ_c is exceeded. The principal stresses are ordered such that $\sigma_I > \sigma_{II} > \sigma_{III}$, with positive stresses acting in tension.

$$\text{Failure will occur if:} \quad \begin{aligned} &\sigma_I \geq \sigma_t, \text{ or} \\ &\sigma_{III} \leq -\sigma_c \end{aligned} \tag{4}$$

Table 1 Summary of material properties [18–23].

Material	OFHC (UNS C10200) copper	CW614N (CZ121) brass	CeramAlox 99.7% alumina	MACOR™
E (GPa)	117	150	370	67
σ_y (MPa)	49.0-78.0	300	-	-
σ_t (MPa)	261-441	430	150	90
σ_c (MPa)	N/A	N/A	2000	345
ν	0.31	0.31	0.23	0.29
c_p * (J/(kg·K))	385	380	900	790
k * (W/(m·K))	385	121	33.0	1.46
α * ($\times 10^{-6}$/K)	17.7	20.9	7.50	9.00
ρ * (kg/m^3)	8900	8470	3950	2520
T_m (°C)	1080	875	1400	1000

D. Simulation and design

1. Methodology overview

The starting point for numerical modeling of the calorimeter is Eq. (1), which provides a nominal value for the stagnation-point heat flux q_0, for a given set of flow properties (K_i, P_0 and h_0) and probe radius of curvature (r). Here, K_i is a thermodynamic property of argon gas, which is found to equal 0.1495 kg/(s·m$^{1.5}$ · atm$^{0.5}$) [5]. Existing simulation data for OPG1 are given in Table 2 - these are used to predict q_0 as a function of r. Note that small values of probe radius, especially those around the OPG1 nozzle exit radius of 7.5 mm, correspond to large surface heat loads - and hence temperature gradients - during flow exposure. These heat loads impose strict upper limits on the exposure time, due to the defined survivability requirements.

Table 2 Simulated flow properties of OPG1 [1].

Parameter	h_0	P_0	M_∞	T_∞
Value	15 MJ/kg	2714 Pa	3	7400 K

The value of q_0 is dependent upon the geometry of the slug and the calorimeter body, as well as the nature of the incident flow. From q_0, it is possible to define other relevant values which are used in analysis and post-processing. Appendix A details the key heat transfer correlations used in the presented methods - the numerical implementation of

*Value taken at 20 °C.

these key equations is summarized in Fig. 1. Preliminary calculations were performed using the commercial software package MATLAB (The MathWorks Inc., Natick, MA, USA), with subsequent finite element (FE) models investigated using the software package COMSOL Multiphysics (COMSOL Inc., Burlington, MA, USA). From these FE models, the temperature-time (T-t) response of the slug can be simulated, which is used to evaluate the performance of the calorimeter.

The same solver configuration is used for all FE models, with the same mesh being used for both heat transfer and solid mechanics calculations in each case. For the heat transfer physics, the temperature field is linearly discretized, and the Parallel Direct Solver (PARDISO) type is used with its default settings. For the mechanical model, quadratic serendipity elements are used, and the Multi-frontal Massively Parallel Sparse (MUMPS) direct solver is used with its default settings. These two calculation steps are segregated and performed sequentially, in order to improve computation times and stability. Triangular/tetrahedral elements are used for 2-D/3-D meshes respectively.

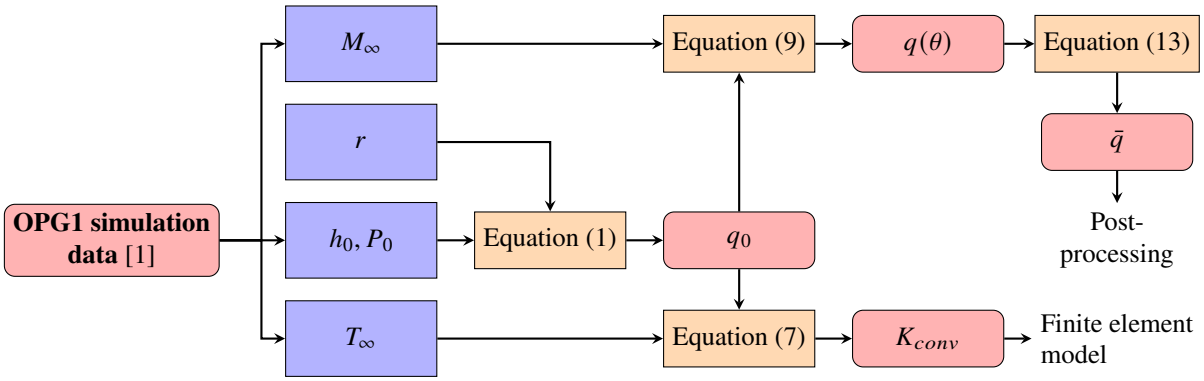

Fig. 1 Overview of preliminary calculations.

ASTM Standard E457 defines two criteria by which the performance of the slug calorimeter is assessed, both of which are based upon the temperature-time (T-t) data gathered. The first of these criteria is the predicted value of the surface heat flux defined by Eq. (2) which is the slug surface-averaged heat flux $\bar{q}$ for the hemispherical calorimeter present in this design. The value of temperature gradient $\frac{\partial T}{\partial t}$ must be obtained within the range of times τ specified by Eq. (5), based upon the length L of the slug and its thermal properties. Conveniently, this condition is satisfied by the 99% rise time t_{99} of the slug, defined by Eq. (6).

$$\frac{L^2 \rho c_p}{2k} < \tau < \frac{L^2 \rho c_p}{k} \tag{5}$$

$$t_{99} = \frac{\ln 200}{\pi^2} \left(\frac{L^2 \rho c_p}{2k} \right) \approx 0.54 \left(\frac{L^2 \rho c_p}{2k} \right) \tag{6}$$

The second performance criterion of concern is the amount of heat loss from the slug, which should be minimized in order to limit measurement errors. The standard method for estimating the magnitude of these losses is to record the slug temperature for some time after exposure to the heat source has ceased - the energy balance described by Eq. (2) can then be used, this time with the temperature gradient as the slug begins to cool. If the magnitude of this value is less than or equal to 5% of the predicted heat flux value from the 'heating' portion of the slug T-t curve, then the heat losses from the slug are considered acceptable.

These two criteria form the basis for an energy-based model of the slug temperature response, which assumes that heat losses are negligible. This shall henceforth be referred to as the 'ASTM method', as this is the method of heat flux prediction stipulated by ASTM Standard E457. The alternative 'Loss model' presented by Hightower et al. [15] shall also be used with the T-t curves of each calorimeter model to provide an additional estimate for the surface heat flux. This model is applied using the methodology described in Ref. [15], with the coefficient of determination R_2 used to measure the 'goodness of fit' between the model and the dataset to which it is applied.

2. Validation case

Given the similarity of the OPG1 calorimeter design to the work of Raybon et al. [13], along with the fact that the authors used the same software during their design process, it was decided that the work of these authors could be used to help validate the methodology used in our work. This is done by independently recreating the geometry of the 'Leste' calorimeter based upon the information provided in Ref. [13], and evaluating the performance of this calorimeter under the reported heat loads.

Using the experimentally determined stagnation-point heat flux value of $q_0 = 1.33$ MW/m^2, the presented methodology is applied in an attempt to reproduce the T-t curve presented in Ref. [13]. The resulting finite element data are given in Fig. 2, along with the experimental data presented in Ref. [13], which was digitally transcribed using the Graph Grabber software tool (Quintessa Ltd., Oxfordshire, UK). The data obtained by analyzing these curves using the ASTM method and Loss model are summarized in Table 3.

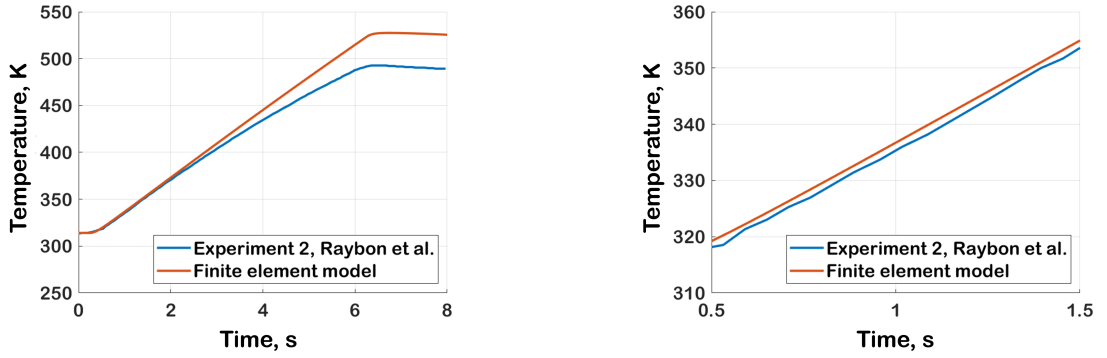

(a) T-t curves. **(b) Close-up of region between t_{99} and 1s + t_{99}.**

Fig. 2 Comparison of numerical and experimental data, for the 'Leste' calorimeter.

From Fig. 2b, it is observed that the FE model provides a close fit to the experimental data from Ref. [13] within the range of times 0.5s $< t <$ 1.5s. This corresponds to the time range from which the average heating slope is taken, therefore indicating that the FE model will likely give a close match to the reported surface heat flux. At higher values of t, the FE model diverges from the experimental data, likely due to the assumption that some physical properties of the materials used remain constant with temperature, which was found to influence the temperature response in Ref. [13].

The data in Table 3 show that the FE model predicts slightly higher values for the surface heat flux than the reported experimental value, with the Loss model estimating a higher value than the ASTM method. Here, the heating slopes are measured between 0.5s and 1.5s, and the cooling slopes are taken between 7s and 8s. The properties of OFHC copper are taken from Ref. [13] - note that these differ from those shown in Table 1. Although there is a small difference in the predicted heat flux, these findings show that the FE model is in good agreement with the data presented by the authors. Application of the same analyses to the T-t curve presented in Ref. [13] gives a steeper heating slope than is reported, which indicates that there has likely been an error when digitally transcribing the graphical data from this paper.

Table 3 Summary of the analyzed T-t curves for the 'Leste' calorimeter geometry.

Dataset	Heating slope (K/s)	Cooling slope (K/s)	Heat losses (%)	q_0 (MW/m^2)	
				ASTM method	Loss model
Experiment 2 (as reported in Ref. [13])	35.2	-1.3	3.75	1.33	-
Experiment 2 (recreated from temperature curve)	36.4	-2.02	5.56	1.49	1.48
FE model	35.7	-1.78	4.99	1.36	1.40

In Ref. [13], it is reported that the mullite insulator fractured during the first test run, in which the calorimeter measures a surface heat flux of 2.53 MW/m^2. It is also reported that the ceramic does not fracture for the second test

run, which features 8s of exposure to a surface heat flux of 1.33 MW/m^2. Using the same values of surface heat flux in the FE model indicates that the first principal stress developed within the ceramic insulator exceeds its tensile strength, which is taken as 132 MPa [24]. However, this occurs within 3s of exposure for both test conditions, indicating that the FE model used is likely conservative. Figure 3 shows the first principal stress at this time for the two test conditions.

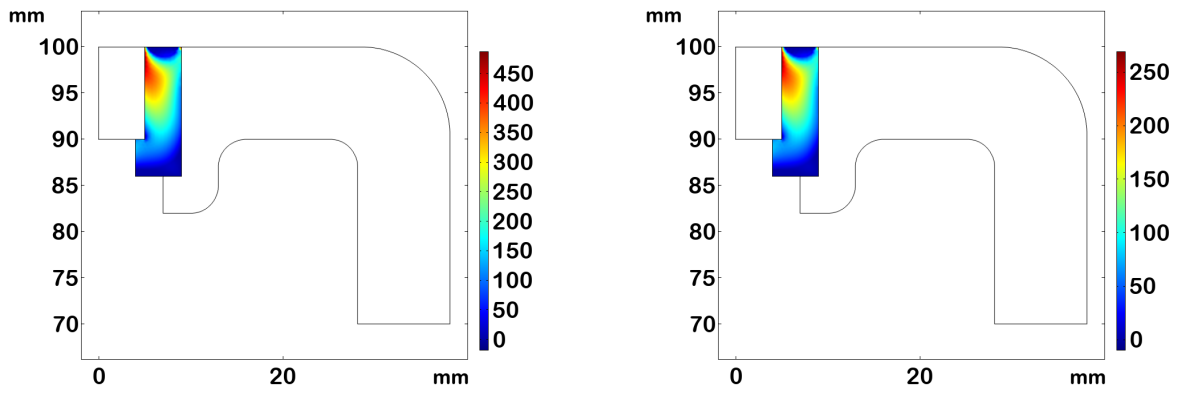

(a) Experiment 1. **(b) Experiment 2.**

Fig. 3 First principal stress (MPa) within the mullite component of the 'Leste' calorimeter after 3s of exposure, from the FE model.

3. Calorimeter model

Figure 4 shows the 15mm diameter calorimeter assembly. It was decided to use three K-type thermocouples (OMEGA Engineering, GG-K-SLE-36) to gather more information about the propagation of heat flux through the slug. One thermocouple is connected directly to the rear face of the slug, as specified by ASTM Standard E457, with the other two embedded at distances of 2.50mm and 4.00mm from the rear face, to measure the temperature near the center and front face of the slug respectively.

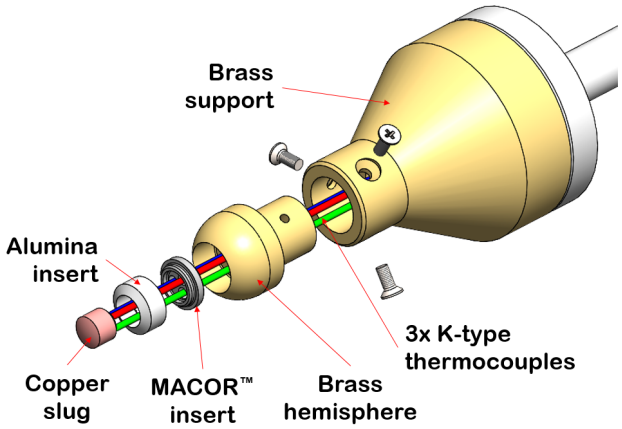

Fig. 4 Exploded view of the calorimeter assembly.

To improve the available exposure time of the calorimeter, it was decided to use two separate ceramic pieces to insulate the slug. The rear of the slug is insulated by a MACOR™ disc, with a small raised edge to center the slug within its support. The sides of the slug are insulated by an alumina piece, with a thin layer of stagnant argon between the outside of the slug and the inner face of the alumina. The alumina provides a moderate level of insulation between the slug and the calorimeter body, while also offering a higher volumetric heat capacity ($= \rho c_p$) than both brass and MACOR™ - this can be inferred from Table 1. Along with its high maximum temperature, this allows the alumina piece to effectively withstand the high surface heat loads near the stagnation point, as shown in Fig. 5.

Numerical analyses were conducted on a three-dimensional (3-D) FE model of the calorimeter with some asymmetries. The mesh features $n = 4.4 \times 10^5$ tetrahedral elements, with an average element quality of 0.642. In order to validate mesh independence, a mesh convergence study was performed with a finer mesh of $n = 1.4 \times 10^6$ elements. The simulated thermocouple T-t curves were used as a convergence metric, as these indicate the performance of the calorimeter. The relative temperature difference between these two sets of results remained within 1.5% over the time range of concern, which is considered to be acceptably low. Therefore, mesh independence is said to be achieved, as the accuracy gained by refining the mesh is considered negligibly small.

Examples of the temperature field within the 15mm calorimeter are shown in Fig. 5, with the temperature response of the slug shown and analyzed in Fig. 6. The plasma source is 'switched on' at $t_1 = 1$s and 'switched off' at $t_2 = 3$s. The heating and cooling slopes are taken at $t = 1.12\text{s} \approx t_1 + t_{99}$ and $t = 3.5$s respectively, where the latter of these values is slightly higher than $t_2 + t_{99}$ due to the late peak in the T-t curve.

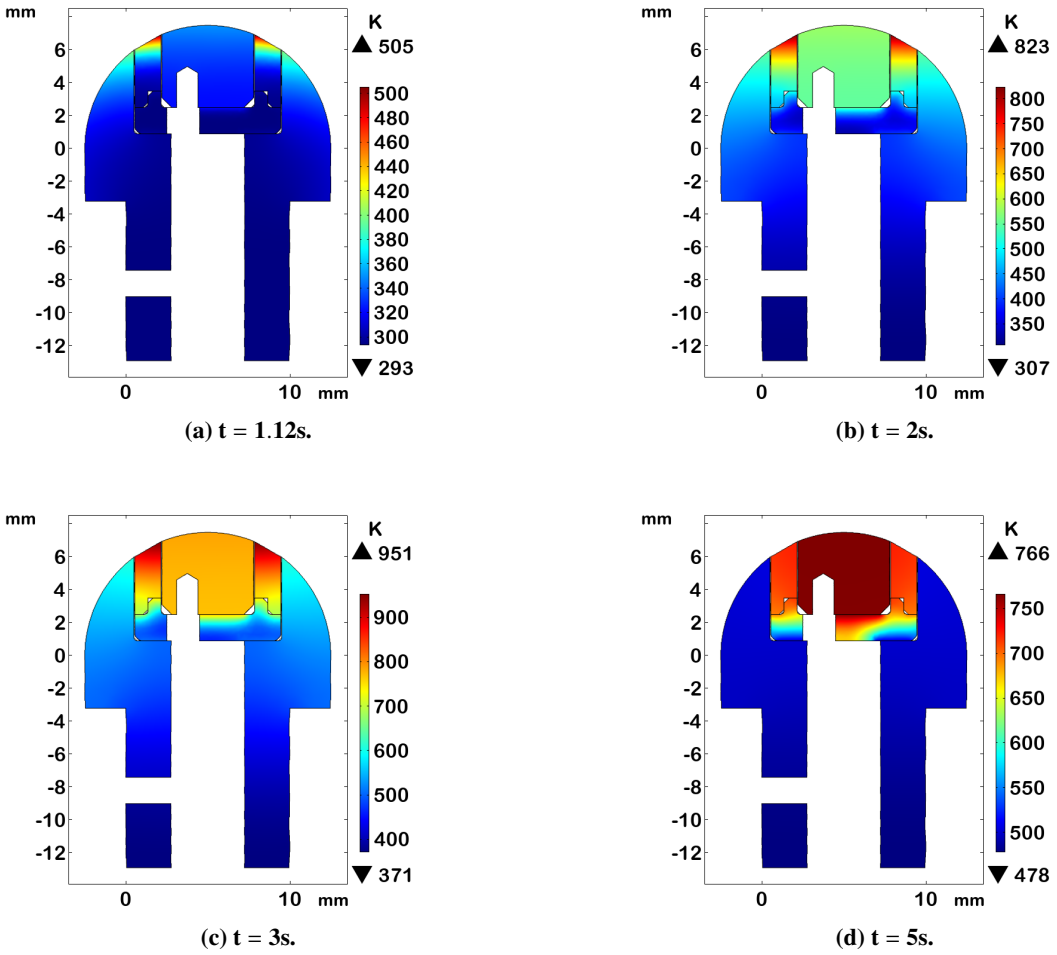

(a) t = 1.12s. **(b) t = 2s.**

(c) t = 3s. **(d) t = 5s.**

Fig. 5 Temperature (K) within the FE model.

The ASTM method gives a predicted heat flux of 3.75 MW/m^2, with heat losses as approximately 3.97% of this value. These heat losses are within the ± 5% tolerance band specified by ASTM Standard E457, which indicates that losses from the slug are acceptably small. The Loss model, applied between the black dotted lines shown, gives a predicted heat flux of 3.82 MW/m^2, with $R_2 = 1.000$. The error of the predicted heat flux is −7.05% for the ATSM method, and −5.33% for the Loss model, relative to the nominal value of $\bar{q} = 4.03$ MW/m^2. These errors are considered to be acceptable, as both are within ± 10%.

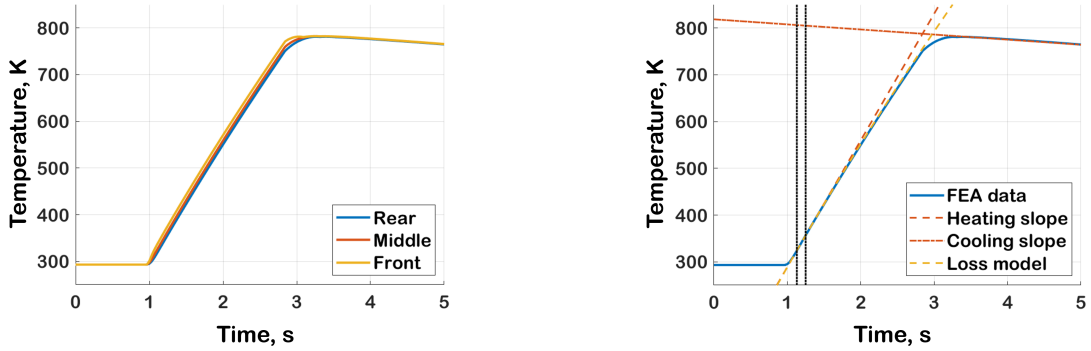

(a) Temperature data from finite element model. **(b) Application of ASTM method and Loss model.**

Fig. 6 Heat loss analysis of the calorimeter FE model.

Figure 7 shows examples of the temperature distributions within the slug, with isothermal contours shown. Note that the isothermal contours near the exposed front face of the slug are almost planar during flow exposure - this means that the net heat flows within the slug are almost one-dimensional in the downwards direction, indicating that the sides of the slug are well-insulated. The isothermal contours become distorted near the tips of the two thermocouple bore holes, however these distortions appear to be highly localized, with the isothermal contours becoming more planar in the middle and rear of the slug. The high degree to which these distortions are localized indicates that the presence of each bore hole has a negligible effect upon the temperature readings of other thermocouples. At t = 5s, the temperature within the slug is uniform to within 1.5K, and the influence of radiative losses at the front face are more pronounced - this is seen in the curved red contours of Fig. 7b.

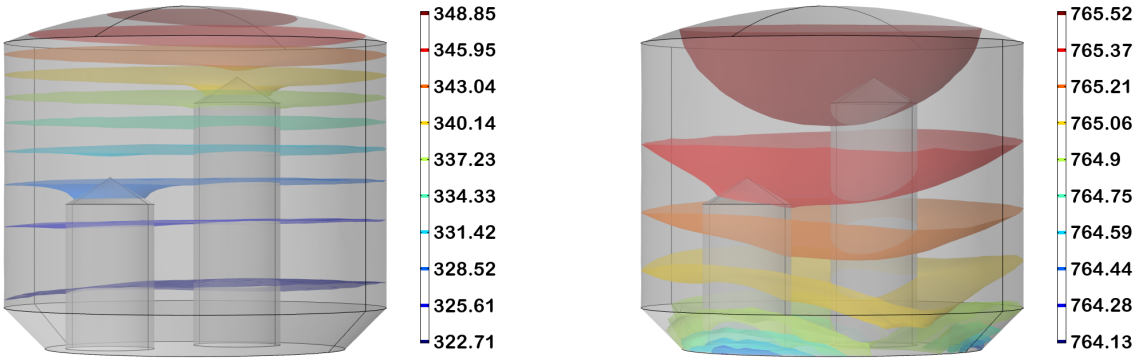

(a) t = 1.12s. **(b) t = 5s.**

Fig. 7 Temperature (K) within the slug of the FE model.

Figure 8 shows the volumetric strain within the brass hemisphere, at peak heating and 2s after exposure has ceased. The largest strains of 1.91% are sufficiently low to indicate that the calorimeter body would not undergo a large thermal expansion during flow exposure. This means that any changes to the probe geometry during the exposure time are negligible, as are the effects of these changes upon the flow field around the calorimeter.

The 'stress-equivalent' strain within the calorimeter body is shown in Fig. 9. The displacement field is constrained with roller constraints normal to the inner surfaces of the bolt holes. Towards the end of exposure, and after exposure has ceased, there are highly localized regions of yielding (shown in magenta) around the bolt holes - this is considered to be a modeling artefact due to the displacement constraints used. Furthermore, it should be noted that if yielding were to occur, then the brass would exhibit some ductility and strain-hardening, hence delaying a critical failure.

(a) t = 3s. **(b) t = 5s.**

Fig. 8 Volumetric strain (%) within the FE model.

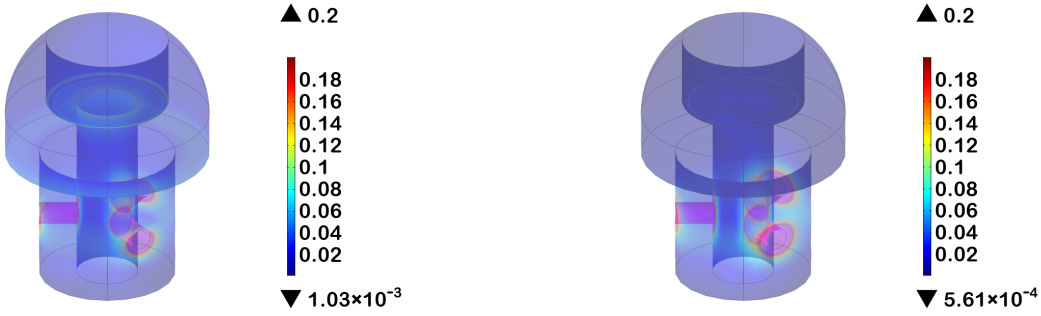

(a) t = 3s. **(b) t = 5s.**

Fig. 9 'stress-equivalent' strain (%) within the FE model.

Figures 10 and 11 show the principal stresses σ_I and σ_{III} respectively in the rear insulation - note that positive values are tensile. These results indicate that the MACOR™ is expected to fail in tension after exposure has ceased, likely due to the high temperature gradients shown in Fig. 5d. However, the presence of an adhesive has not been considered in this model - this will be present in reality, and would dissipate some of the fracture energy before this component breaks. The results indicate that the component is unlikely to fail in compression.

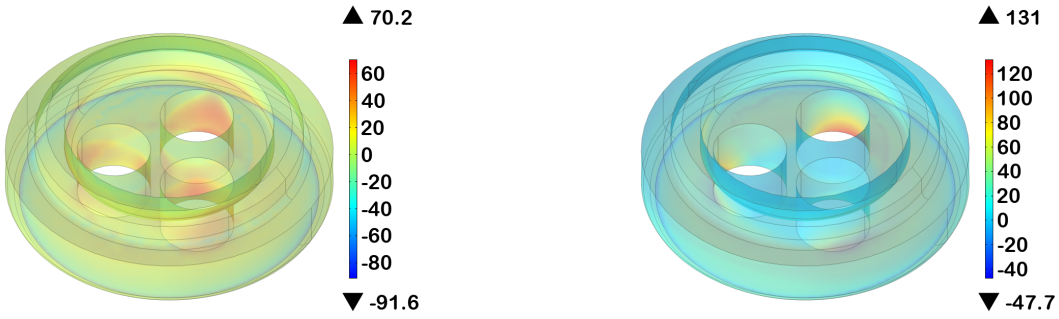

(a) t = 3s. **(b) t = 5s.**

Fig. 10 First principal stress (MPa) within the MACOR™ component of the FE model.

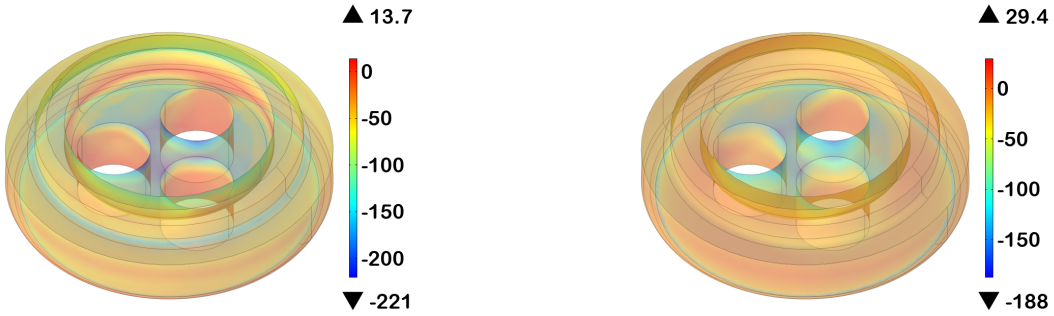

(a) t = 3s. **(b) t = 5s.**

Fig. 11 Third principal stress (MPa) within the MACOR™ component of the FE model.

For the purpose of reduced computation times, the alumina side insulation is not considered in the mechanical simulations shown here. However, it was analyzed in this manner in a simpler, 2-D axisymmetric model of the calorimeter, the results of which indicate that the stresses in the alumina were low. Given that the real alumina piece is also axisymmetric, it is assumed that the stresses for the 2-D and 3-D models are similar.

Although these results indicate that mechanical failure may occur in some components, the associated risk is considered to be acceptably low for the design to be considered satisfactory. It should also be noted that this analysis is thought to be highly conservative, based upon the findings of the validation case.

Based upon the presented simulation results, this model is deemed to satisfy the performance criteria described in Section II. As of writing, the 15mm calorimeter design shown in Fig. 4 has been manufactured and assembled. Engineering drawings for three geometrically similar calorimeters have also been made, which have outer diameters of 20mm, 25mm and 35mm. The purpose of these designs is to ascertain the performance of the base calorimeter design at lower heat loads, and to provide some contingency in the event of a failure.

IV. Total pressure probe

A. Simulation and design

It was decided to use a pressure transducer to measure the stagnation pressure P_0 of the plasma flow. This sensor is housed within the shielding inside the vacuum chamber of OPG1, and is connected to a hemispherical probe body by a sealed tubing framework. Mounting the transducer inside the vacuum chamber allows for the internal volume of the 'channel' formed by the tubing framework to be minimized. This reduces the response time required for the pressure at the sensing area of the transducer to reach equilibrium with the pressure at the stagnation point of the flow.

Figure 12 shows the assembly model of the total pressure probe, with the pressure transducer mounted horizontally in the shielded housing structure. Based upon the pre-defined geometry of the sting, the diameter of the hemispherical body is chosen to be 35mm, which is equal to the flange diameter of the central rod. Given that the stagnation pressure is an intrinsic property of the plasma flow, it is independent of the probe geometry used. Therefore, unlike the calorimeter design presented in Section III, it is considered beneficial in this case to use a probe with larger diameter, as this will increase the available exposure time of the total pressure probe.

To ensure its structural integrity, and to estimate the available exposure time, the total pressure probe design is analyzed using the same numerical methods described in Section III. Given that the flow is only incident on the front face of the probe, only this component and the central rod is analyzed, with the latter used to constrain the displacement field in the assembly. These components are modeled as axisymmetric, under the assumption that the four bolt holes will have a negligible effect upon the temperature and displacement fields. This assumption has been verified by the similarities between the 2-D and 3-D calorimeter models presented. Figure 13 shows the geometry of the model used, alongside the mesh featuring $n = 3,030$ triangular elements.

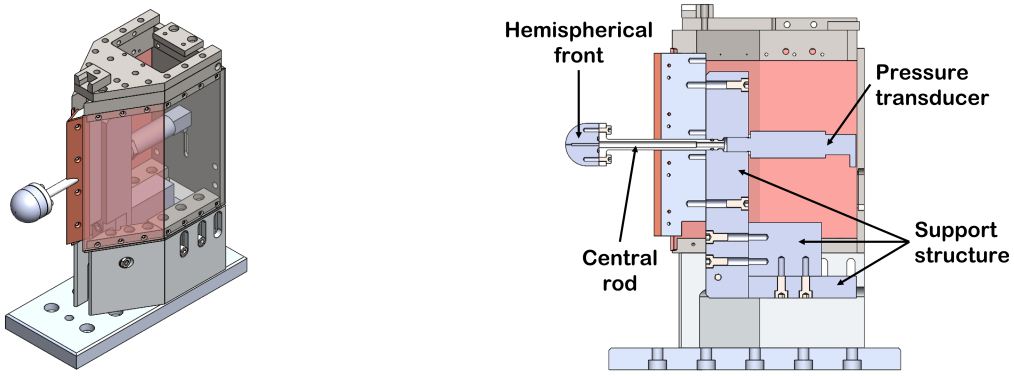

(a) Isometric view. **(b) Cross-sectional view.**

Fig. 12 Assembly drawing of the total pressure probe.

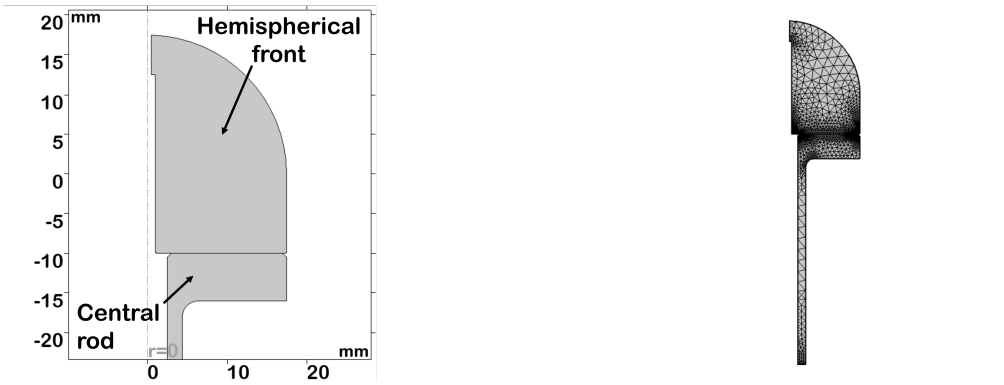

(a) Overview of geometry used. **(b) Mesh with n = 3,030 elements.**

Fig. 13 Overview of the 2-D total pressure probe model.

The materials used for the hemisphere and rod are C614N brass and 304 stainless steel respectively. The properties of 304 stainless steel at 20 °C are given in Ref. [25], and their temperature-dependence is already modeled in a preset material ('304 [solid, oxidized]') within the COMSOL material library - this material preset was used in the following numerical methods. Recall that the properties of CW614N brass are summarized in Table 1. The results of a time-dependent heat transfer study are presented in Fig. 14. This analysis uses the same procedure and solver configuration as the heat transfer analyses for the calorimeter. It is assumed that the flow is 'switched on' at $t_1 = 1$s, and that $t_2 > 20$s. The surface heat flux $q(\theta)$ for a flow incident on a 35mm diameter hemisphere are is described by Eqs. (1) and (9), based upon the test conditions specified in Table 2. From Eq. (7), it is found that $K_{conv} = 390$ W/(m^2·K), which is used in the FE model. The value corresponding to $q(\theta = \frac{\pi}{2})$ is then applied along the side edges of the front piece, and the sides of the flange on the central rod. It is assumed that the surface heat flux upon the sides of the rod that are downstream of the flange is negligible, given that they are far-removed from the plasma flow. Radiative effects are included on all exposed surfaces in the model, with the surface emissivity of the hemisphere and central rod taken to be 0.2 and 0.7 respectively. These values have been chosen under the assumption that the brass hemisphere is polished, and the stainless steel rod is unpolished and oxidized. The rear of the central rod, as well as any internal surfaces within the assembly, are assumed to be perfectly thermally insulated.

The exposure time of the total pressure probe is limited by the thermal of mechanical failure of either component. Thermal failure will occur if either of the components begins to melt, which is more likely to occur in the brass hemisphere than the steel central rod, due to the combination of higher average surface heat flux and lower melting temperature (see Table 1 and Ref. [25]). From Fig. 14, it appears that exposure times of up to approximately 18s may be achievable for the test condition specified, if the brass melting temperature of 850 °C (= 1123 K) is used as the maximum acceptable temperature.

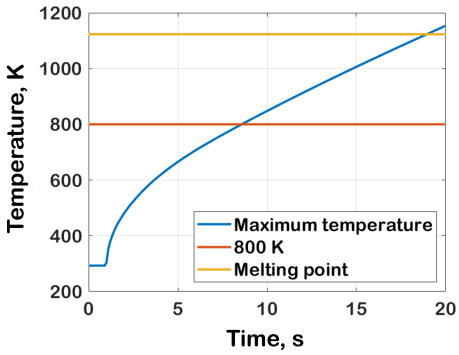

Fig. 14 Maximum temperature of the brass hemisphere in the total pressure probe.

A mechanical analysis was conducted, using the same procedure and solver configuration as the mechanical analyses for the calorimeter. The displacement field is rigidly constrained at the bottom face of the central rod, with all internal and external surfaces free. The 'stress-equivalent' strain within the probe assembly does not exceed 0.15% for any of the times investigated. The yield criterion of 0.2% strain is applicable to both the brass and steel components here, based upon the definition of yield stress for both metals. Therefore yielding due to thermal expansion is unlikely to occur.

B. Response time analysis

In the presented design for the total pressure probe assembly, the sensing area of the pressure transducer is not located at the stagnation point of the flow field. The distance between these two locations results in a finite response time, during which the pressure at the front face of the transducer is not in equilibrium with the stagnation point pressure. Assuming the incident plasma flow is supersonic, this response time can be determined by consideration of the isentropic flow relations, as these govern the behavior of the weak pressure waves that will propagate from the stagnation point to the transducer front face. The total response time of the system is then the sum of the 99% rise time t_{99}, the pressure wave propagation time t_p, and the response time of the sensor used, which is quoted as 1ms by the manufacturer [26]. This gives a total response time of 2.93ms, which is much lower than the available exposure time, indicating that it will not be a limitation during testing. The details of this analysis are provided in Appendix B.

V. Preliminary results

Figure 15a shows the finished parts for the 25mm diameter slug calorimeter - named 'OPG1-CALPROBE25' - with the fully assembled probe shown in Fig. 15b. The thermocouple beads were attached to the slug with a high-conductivity silicon-based sealant, with a commercially available high-temperature cement [27] used to ensure structural integrity at high temperatures. Where necessary, the components were glued together with RESBOND™ 989, which is a general-purpose alumina-based sealant with a low thermal conductivity [28].

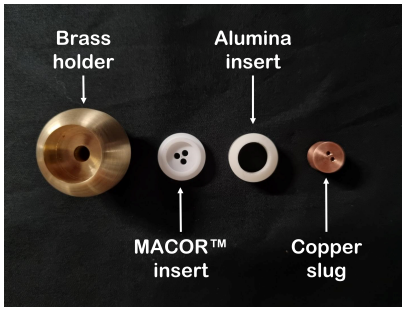

(a) Finished components.

(b) Assembled calorimeter.

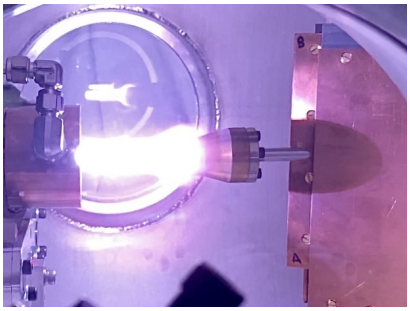

(c) Calorimeter during testing.

Fig. 15 'OPG1-CALPROBE25' assembly.

The calorimeter has been tested under various combinations of flow conditions, across multiple successful test runs of OPG1. Four of these test runs produced stable supersonic flows, the conditions for which are presented in Table 4. During these runs, the distance between the front face of the slug and the nozzle exit was 50mm, and the calorimeter was left to cool before commencing the next run. Figure 16 gives the resulting T-t curves recorded by the calorimeter, where TC1, TC2 and TC3 correspond to the thermocouples embedded at the front, center and rear face of the slug respectively. It is thought that the slow response of TC3 compared to the other thermocouples is due to the low thermal conductivity of the glue and cement used.

Table 4 Conditions used for test runs in OPG1.

Run Number	Average argon flowrate (L/min)	Arc current (A)	Average chamber pressure (Pa)
1	8.171	40	1909
2	11.13	80	1827
3	11.15	60	2703
4	10.90	60	1710

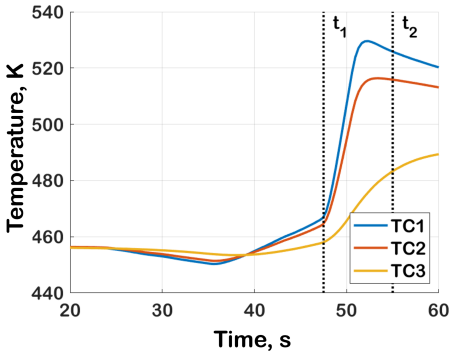

(a) Run 1.

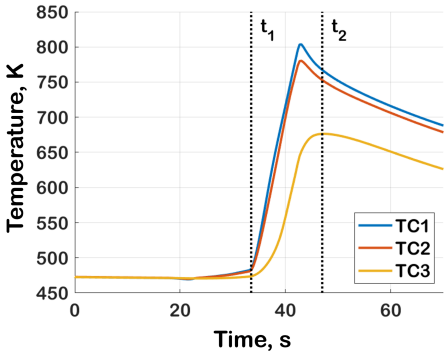

(b) Run 2.

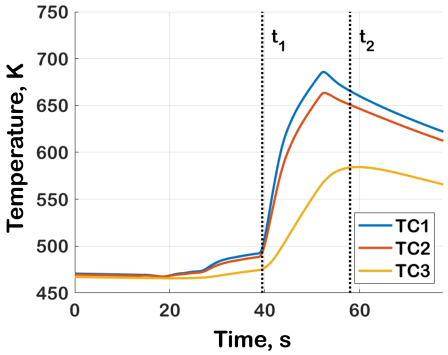

(c) Run 3.

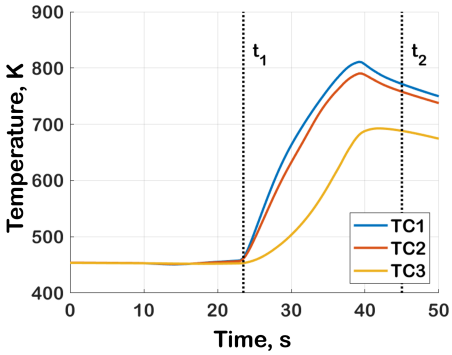

(d) Run 4.

Fig. 16 Temperature measurements of the calorimeter in OPG1.

The TC2 T-t curves shown in Fig. 16 are analyzed using the ASTM method and Loss model, with the results presented in Table 5. The times t_1 and t_2 are chosen at points where the temperature curve first becomes linear, in its heating and cooling regions respectively. t_1 is taken after the initial flow establishment time, during which the

stagnation-point heat flux is small relative to that during the established flow. In each case, the data in the following 2s period is considered. Although this time range is inconsistent with Eq. (5), it must be noted that the thermocouple sampling rate for the current data acquisition system is limited to approximately 3Hz per thermocouple. Therefore, this measurement period ensures that a sufficient number of temperature readings are analyzed, within a wholly linear region of the T-t curve. The data from TC2 is analyzed as this corresponds to the temperature in the center of the slug, which is representative of the volume-average implied by Eq. (2).

From Eq. (2), the value of $\bar{q}$ is subject to uncertainties in the values of A, V, ρ, c_p and T. From the slug manufacturing tolerances, $V = 496.16 \pm 4.47$ mm^3 and $A = 69.53 \pm 2.32$ mm^2. The uncertainty in TC readings are taken as 0.8% of the temperature, according to the specifications of the data acquisition system [29]. Uncertainties for the material properties are unknown, hence are neglected.

The estimated heat losses given by the ASTM method vary considerably between each test case. Only the T-t curve from Run 1 indicates that the losses from the slug are within the ±5% tolerance range specified by ASTM Standard E457, with the other test runs indicating unacceptable heat losses. When comparing these values to the data in Fig. 16, it appears that the heat losses during cooling depend upon the temperature of the slug when the flow is switched off. At higher temperatures, the cooling slope seems to be lower, which is thought to be due to high radiative losses from the alumina insert. This would quickly reduce the average temperature of the alumina after the flow has ceased, hence increasing the heat losses from the side of the slug. Also, the slug has likely experienced some convective heat loss, due to the pressure in the vacuum chamber being greater than expected. The ASTM method and Loss model yield similar values for the heat flux in each test run. There are high uncertainties associated with the calculated heat flux values. These could be reduced by accurately measuring the mass of the slug before installation in the calorimeter.

Table 5 Analyzed data from OPG1-CALPROBE25.

Run Number	ASTM method				Loss model		Uncertainty in $\bar{q}$ (%)
	Heating slope (K/s)	Cooling slope (K/s)	$\bar{q}$ (MW/m^2)	Estimated losses (%)	$\bar{q}$ (MW/m^2)	R_2	
1	14.22	-0.5475	0.3710	3.850	0.3635	0.9966	± 27.9
2	31.42	-4.649	0.8230	14.79	0.8024	0.9945	± 15.6
3	22.33	-2.097	0.5844	9.389	0.5745	0.9951	± 15.8
4	28.01	-4.126	0.7321	14.73	0.7289	0.9991	± 13.2

From Eq. (13), the slug geometry gives $q_0 = 1.05\bar{q}$, allowing for the estimation of the stagnation-point heat flux for each run. Figure 17 shows the relationship between predicted heat flux and arc current for the test runs analyzed. Although the argon mass flowrate and vacuum pressure change between runs, these values are considered consistent enough for a direct comparison. It is expected that the heat flux increases linearly with increasing arc current (assuming a constant mass flow rate of argon), with a y-intercept at the origin. The line of best fit shown indicates that the analyzed data follows this trend, however it should be noted that this best fit is based on a very small dataset. The collection of data across a wider range of test conditions is required to corroborate these results.

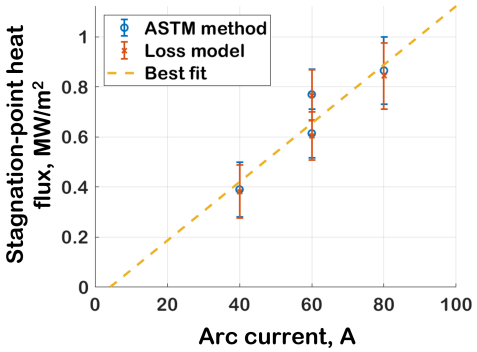

Fig. 17 Scatter plot of estimated heat flux data.

VI. Conclusions

The designs for a complete set of calibration instrumentation for OPG1 are presented. This incorporates a slug calorimeter to measure the stagnation-point heat flux rate of the flow, and a total pressure probe.

Numerical analyses of the slug calorimeter design indicate heat losses of approximately 3.97% from the slug, which is considered to be acceptably low. The mechanical response of the calorimeter was also investigated to ensure its structural integrity. This highlighted the fracture of the ceramic insulators as a possible concern, however given the highly conservative nature of these analyses, it was decided that the design was still satisfactory. The methodology used is compared to the data in Ref. [13], and is found to agree with these findings.

Numerical analyses of the total pressure probe design indicate that exposure times of up to approximately 18s are achievable before the brass front of the probe melts. It is found that mechanical failure of the probe is unlikely to occur. A response time analysis, based upon the principles of isentropic flow, indicates a system response time of approximately 3ms, which does not limit the sensing capabilities of the device.

Based upon the presented designs, a total pressure probe has been manufactured, along with four different sizes of slug calorimeter. Preliminary experimental data for the 25mm calorimeter are presented and analyzed, and indicate higher slug heat losses than expected, which is thought to be due to high vacuum chamber pressures. The measured stagnation-point heat flux is thought to increase linearly with arc current, up to a maximum value of 0.85 MW/m^2 for an arc current of 80 A. The other devices have not yet been used in the facility, but are planned to be in the near future. This will allow for the first enthalpy estimations for this facility to be made.

Some improvements to the infrastructure of the OPG1 facility, such as upgraded vacuum pumps, data acquisition system and a traverse system, are already planned. These upgrades will allow for improved testing capabilities and more accurate flow characterization, and will allow better determination of the heat losses from the slug calorimeter. The calorimeter design is also planned to be calibrated using a heated flow Venturi tube rig, in order to better quantify its performance. Use of the other calorimeter sizes within the facility will allow for testing across a wider scope of conditions.

Acknowledgments

This research was funded in whole by the UKRI Future Leaders Fellowship scheme (grant number MR/T041269/1) and we extend our gratitude to UKRI. For the purpose of Open Access, the author has applied a CC BY public copyright license to any Author Accepted Manuscript (AAM) version arising from this submission.

References

[1] Hermann, T., Chang, E., Schäfer, J., Joglekar, C., and Böhrk, H., "Development of Small Scale Arc-jet Facility OPG1," *AIAA SciTech 2023 Forum*, American Institute of Aeronautics and Astronautics Inc, AIAA, National Harbor, MD, 2023. https://doi.org/10.2514/6.2023-2331.

[2] Chang, E., Valeinis, O., Schäfer, J., and Hermann, T., "Commissioning of the OPG1 Plasma Wind Tunnel," *34th International Symposium on Shock Waves*, International Shock Wave Institute, ISWI, Daegu, Korea, 2023. Unpublished.

[3] Kolesnikov, A. F., "Extrapolation from High Enthalpy Tests to Flight Based on the Concept of Local Heat Transfer Simulation," *Measurement Techniques for High Enthalpy and Plasma Flows*, NATO Research and Technology Organisation (RTO), von Kármán Institute for Fluid Dynamics (VKI), Rhode-Saint-Genése, Belgium, 1999. URL https://www.sto.nato.int/publications/STO%20Educational%20Notes/RTO-EN-008/EN-008-\protect\T1\textdollar\protect\T1\textdollarTOC.PDF.

[4] Fay, J. A., and Ridell, F. R., "Theory of Stagnation Point Heat Transfer in Dissociated Air," *Journal of the Aeronautical Sciences*, Vol. 25, 1958, pp. 73–85, 121. https://doi.org/10.2514/8.7517.

[5] Sutton, K., and Graves, R. A., "A General Stagnation-Point Convective-Heating Equation for Arbitrary Gas Mixtures," , 1971. URL https://ntrs.nasa.gov/citations/19720003329, NASA report.

[6] Auweter-Kurtz, M., Kurtz, H. L., and Laure, S., "Plasma generators for re-entry simulation," *Journal of Propulsion and Power*, Vol. 12, 1996, pp. 1053–1061. https://doi.org/10.2514/3.24143.

[7] ASTM Standard E637-22, 2022, *Standard Test Method for Calculation of Stagnation Enthalpy from Heat Transfer Theory and Experimental Measurements of Stagnation-Point Heat Transfer and Pressure*, ASTM International, West Conshohocken, PA, 2022. https://doi.org/10.1520/E0637-22.

[8] ASTM Standard E422-22, 2022, *Standard Test Method for Measuring Net Heat Flux Using a Water-Cooled Calorimeter*, ASTM International, West Conshohocken, PA, 2022. https://doi.org/10.1520/E0422.

[9] ASTM Standard E457-08, 2020, *Standard Test Method for Measuring Heat-Transfer Rate Using a Thermal Capacitance (Slug) Calorimeter*, ASTM International, West Conshohocken, PA, 2020. https://doi.org/10.1520/E0457-08R20.

[10] ASTM Standard E459-22, 2022, *Standard Test Method for Measuring Heat Transfer Rate Using a Thin-Skin Calorimeter*, ASTM International, West Conshohocken, PA, 2022. https://doi.org/10.1520/E0459.

[11] Leiser, D., Hufgard, F., Duernhofer, C., Löhle, S., and Fasoulas, S., "Theoretical and Experimental Analysis of Flight-to-Ground Scaling for Axisymmetric and Planar Bodies," *AIAA Journal*, Vol. 60, 2022, pp. 6609–6619. https://doi.org/10.2514/1.J062055.

[12] Esposito, A., Rosa, F. D., Caso, V., and Parente, F., "Design of Slug Calorimeters for Re-entry Tests," , 04 2023. URL https://www.researchgate.net/publication/266097865.

[13] Raybon, I., Viganò, D., Hamilton, B., and Maddalena, L., "Ceramic Insulated Slug Calorimeter for High-Enthalpy Flows," *Journal of Thermophysics and Heat Transfer*, Vol. 36, 2022, pp. 342–350. https://doi.org/10.2514/1.T6304.

[14] Nawaz, A., and Santos, J., "Assessing Calorimeter Evaluation Methods in Convective Heat Flux Environments," *10th AIAA/ASME Joint Thermophysics and Heat Transfer Conference*, American Institute of Aeronautics and Astronautics Inc, AIAA, Reston, VA, 2010. https://doi.org/10.2514/6.2010-4905.

[15] Hightower, T. M., Olivares, R. A., and Philippidis, D., "Thermal Capacitance (Slug) Calorimeter Theory Including Heat Losses and Other Decaying Processes," , 2008. URL https://ntrs.nasa.gov/citations/20090008662, NASA report.

[16] Wang, Y., Li, X., Liu, D., and Liu, Y., "Analysis of Two Calculation Methods of Heat Flux Based on Slug Calorimeter," *IEEE Sensors Journal*, Vol. 21, 2021, pp. 1287–1293. https://doi.org/10.1109/JSEN.2020.3019006.

[17] "Fine Wire Duplex Insulated Thermocouple Wire," , 2023. URL https://uk.farnell.com/omega/gg-k-36-sle-50/thermocouple-wire-high-temp/dp/3802634#anchorTechnicalDOCS, Datasheet.

[18] Toulfatzis, A. I., Pantazopoulos, G. A., and Paipetis, A. S., "Fracture behavior and characterization of lead-free brass alloys for machining applications," *Journal of Materials Engineering and Performance*, Vol. 23, 2014, pp. 3193–3206. https://doi.org/10.1007/s11665-014-1096-3.

[19] "Copper and Copper Alloys - Brass - CW614N Brass Rod," , 2023. URL https://www.aalco.co.uk/datasheets/Copper-and-Copper-Alloys-CW614N-Brass-Rod_31.ashx, Datasheet.

[20] "Alumina (Al2O3) – CeramAlox™," , 2023. URL https://precision-ceramics.com/uk/materials/alumina, Datasheet.

[21] "MACOR," , 2023. URL https://www.mindrum.com/ceramics/macor/, Datasheet.

[22] "Oxygen Free Copper – UNS C10200," , 2023. URL https://www.azom.com/article.aspx?ArticleID=6306, Datasheet.

[23] "CZ121 / CW614N - FREE MACHINING BRASS," , 2023. URL https://www.holmedodsworth.com/data-sheets/brass-datasheets/cz121-cw614n-free-machining-brass, Datasheet.

[24] "Mullite," , 2023. URL https://www.mindrum.com/ceramics/mullite/, Datasheet.

[25] "304 Stainless Steel," , 2023. URL https://www.matweb.com/search, Datasheet.

[26] "Honeywell MIPAG1XX002BAAAX Pressure Sensor," , 2023. URL https://uk.farnell.com/honeywell/mipag1xx002baaax/pressure-transducer-absolute-2bar/dp/3643158, Datasheet.

[27] "Black Fire Cement - VITCAS," , 2023. URL https://shop.vitcas.com/bfc-black-fire-cement-310ml.html, Datasheet.

[28] "RESBOND™ 989," , 2023. URL https://www.cotronics.com/catalog/27%20989%20989FS%20989F.pdf, Datasheet.

[29] "NI-9210 - Specifications," , 2023. URL https://www.ni.com/en-gb/shop/model/ni-9210.html.

[30] Lees, L., "Laminar Heat Transfer Over Blunt-Nosed Bodies at Hypersonic Flight Speeds," *Journal of Jet Propulsion*, Vol. 26, 1956, pp. 259–269. https://doi.org/10.2514/8.6977.

[31] Howatson, A. M., Lund, P. G., Todd, J. D., McFadden, P. D., and Smith, P. J. P., *Engineering Tables and Data*, Oxford University Press, 2009.

Appendix A: Numerical methods for heat transfer

Given that q_0 represents a convective heat transfer from the flow to the probe surface, it is convenient to define a corresponding heat transfer coefficient K_{conv}, which is useful for defining boundary conditions in later simulation activity. Equation (7) gives this relationship, where the stagnation-point wall temperature $T_{w,o}$ is assumed to initially be 20 °C, and the free-stream plasma temperature T_∞ = 7400 K is assumed to be constant.

$$q_0 = K_{conv}\left(T_\infty - T_{w,0}\right) \tag{7}$$

For a flow incident on a hemispherical surface, the value of surface heat flux q will decrease with increasing angle θ from the stagnation point, as illustrated in Fig. 18. Here, the angle θ_0 is the angle subtended by the front face of the slug, which is defined as:

$$\theta_0 = \arcsin\left(\frac{d}{2r}\right) \tag{8}$$

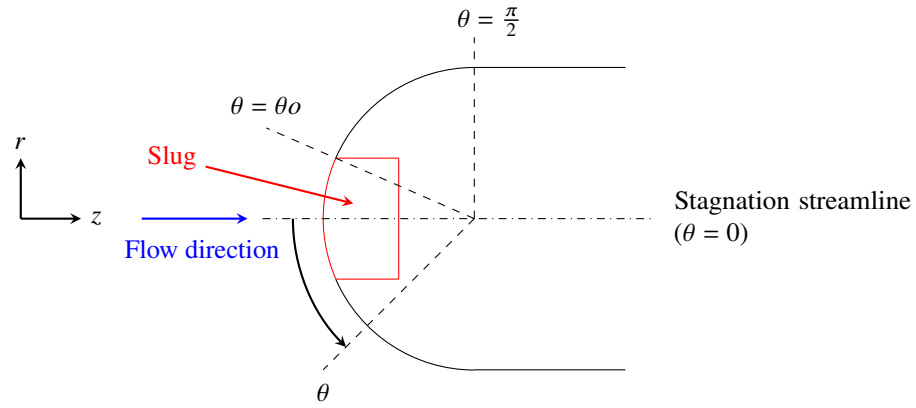

Fig. 18 Definition of θ and θ_0 for a hemispherical slug calorimeter.

The correlation between q and q_0 is described by Eq. (9) [30] - it should be noted that this equation is undefined at $\theta = 0$, which corresponds to the stagnation point at which $q = q_0$.

$$q = q(\theta) = \frac{D_1}{\sqrt{D_2}}\, q_0, \tag{9}$$

where D_1, D_2 are the following functions of subtended angle θ:

$$D_1 = 2\theta \sin\theta \left[\left(1 - \frac{1}{\gamma M_\infty^2}\right)\cos^2\theta + \frac{1}{\gamma M_\infty^2}\right] \tag{10}$$

$$D_2 = \left(1 - \frac{1}{\gamma M_\infty^2}\right)\left[\theta^2 - \frac{\theta}{2}\sin 4\theta + \frac{1}{8}\left(1 - \cos 4\theta\right)\right]$$

$$+ \frac{1}{4\gamma M_\infty^2}\left[\theta^2 - \theta \sin 2\theta + \frac{1}{2}\left(1 - \cos 2\theta\right)\right] \tag{11}$$

with γ = 1.666 representing the heat capacity ratio for argon, and where M_∞ is the free-stream Mach number of the plasma flow field.

Recalling Eq. (2), it is also necessary to calculate the surface average heat flux $\bar{q}$ over the slug's frontal area, as this is the value that will be calculated when using a slug with a curved surface. This can be computed analytically as follows:

$$\bar{q} = \frac{\iint_A q(\theta)\, dA}{\iint_A dA} = \frac{2\pi r^2 \cdot \int_\theta q(\theta)\sin(\theta)\, d\theta}{2\pi r^2 \cdot \int_\theta \sin(\theta)\, d\theta}$$

$$\Rightarrow \bar{q} = \frac{\int_\theta q(\theta)\sin(\theta)\, d\theta}{1 - \cos\theta_0} \tag{12}$$

The integral of $q(\theta)\sin\theta$ is difficult to solve analytically, so is instead computed numerically:

$$\bar{q} = \frac{\int_\theta q(\theta)\sin(\theta)\ d\theta}{1-\cos\theta_0} \approx \frac{I}{1-\cos\theta_0},$$
$$\text{where:} \qquad I = \sum_k^N \frac{1}{2}\left(\frac{\theta_0}{N}\right)\left[q(\theta_k)\sin(\theta_k) + q(\theta_{k+1})\sin(\theta_{k+1})\right], \tag{13}$$

with $N = 100$. Equation (13) allows the quantities q_0 and $\bar{q}$ to be related via a single scale factor. This scale factor is identical for any two geometrically similar slugs, since D_1 and D_2 are both independent of probe radius, and the value of θ_0 would be the same for both cases.

Appendix B: Response time of total pressure probe

The following analysis is based upon changes to the conditions within some downstream volume V to a step change in upstream conditions, where the upstream and downstream regions are connected by a throat of cross-sectional area A_i. It is assumed that the downstream volume is initially at the conditions within the vacuum chamber ($P_v,\ T_v,\ \rho_v$), and that the upstream flow instantly reaches the stagnation-point conditions ($P_0,\ T_0,\ \rho_0$) when the plasma source is switched on. Information is then transferred from the stagnation point to the transducer via the mechanism of weak pressure waves, which propagate downstream at the local speed of sound a. These pressure waves are continuously generated at the throat.

At time t, a weak pressure wave is created at the throat, and begins to propagate downstream. After an infinitesimal time step dt has passed, this pressure wave has moved an incremental distance $dx = a \cdot dt$ from the throat. The conditions in the region behind the wave have changed incrementally, whereas the conditions in the region ahead of the wave are unchanged from time t. The effects that arise from this finite travel time can be modeled by first assuming that the speed of sound is infinitely high, such that the conditions within the entire volume change instantaneously and uniformly. This gives the rise time t_{99} of the system, which is defined as the time taken for the volume V to reach a pressure equal to 99% of P_0. However, the finite speed of sound must then be accounted for, by considering the propagation of the pressure wave produced at t_{99} through the channel. This gives rise to a finite time t_p, which is the time taken for this wave to propagate along the channel length l. The total response time $t_r = t_{99} + t_p$ can then be defined.

The first step in the response time analysis is the calculation of the local Mach number M^* at the throat, in terms of the local speed of sound a and throat flow velocity u^*. Equation (14) gives the definition of a for a fluid, where $R = 208$ J/(kg·K) is the value of the gas constant for argon [31]. Equation (15) gives the value of u^* in terms of the pressure difference between the stagnation point and channel volume, which is based upon the conservation of momentum along the stagnation streamline. Knowing a and u^* allows for the calculation of M^* using Eq. (16), noting that the value of M^* is equal to one if the flow within V is predicted to be supersonic.

$$a = \frac{dx}{dt} = \sqrt{\gamma R T} \tag{14}$$

$$u^* = \sqrt{\frac{2}{\rho_0}(P_0 - P)} \tag{15}$$

$$M^* = \begin{cases} \frac{u}{a}, & \text{if} \quad \frac{u}{a} \leq 1 \quad \text{(Inlet flow is subsonic)}, \\ 1, & \text{if} \quad \frac{u}{a} > 1 \quad \text{(Inlet flow is choked)}. \end{cases} \tag{16}$$

From M^*, it is possible to calculate the incremental mass dm of argon gas that flows into the channel for a given time step dt. This additional mass is assumed to instantly reach equilibrium with the gas already in the volume, hence changing the values of pressure P, temperature T and density ρ at time $t + dt$. Equations (17) to (19) show the relevant isentropic flow relations for this problem, with Eq. (20) based upon the ideal gas law for argon.

$$\dot{m} = \frac{dm}{dt} = A_i P_0 M^* \sqrt{\frac{\gamma}{RT_0}} \left[1 + \frac{1}{2}(\gamma - 1)(M^*)^2\right]^{\frac{-(\gamma+1)}{2(\gamma-1)}} \tag{17}$$

$$P + dP = P\left[1 + \left(\frac{\gamma R T_0}{PV}\right) dm\right] \tag{18}$$

$$T + dT = T\left[\gamma \frac{T}{T_0}\left(\frac{1-P}{P+dP}\right) + \frac{P}{P+dP}\right]^{-1} \tag{19}$$

$$\rho + d\rho = \frac{P + dP}{R(T + dT)} \tag{20}$$

Using Equations (14) to (20) sequentially for a given time step dt yields the conditions in the channel volume at time $t + dt$. This process is repeated until $P \geq 0.99P_0$, which occurs at time $t = t_{99}$.

As argon flows from the stagnation point into the channel volume, weak pressure waves will be continuously generated at the throat. Therefore, it is necessary to account for the pressure wave that is generated at t_{99}, as this will take some finite time $t_p = l/(a|_{t=t_{99}})$ to travel along the channel.

Table 6 gives the geometric properties of the channel shown in Fig. 12. The throat is located at the front of the hemispherical piece, as this is the point in the channel with the smallest cross-sectional area. Also presented are the predicted conditions at the stagnation-point and within the vacuum chamber (from Ref. [1]), where $T_v = 293.15$ K is assumed. The values of density are calculated from the temperature and pressure using the ideal gas law for argon.

Table 6 Summary of values for response time analysis.

Channel geometry			**Stagnation point conditions**			**Vacuum chamber conditions**		
V (mm^3)	A_i (mm^2)	l (mm)	P_0 (Pa)	T_0 (K)	ρ_0 (kg/m^3)	P_v (Pa)	T_v (K)	ρ_v (kg/m^3)
1934	0.79	130.5	2714	7400	2.0×10^{-3}	125	293.15	1.8×10^{-3}

The results of this analysis are shown in Fig. 19. Figure 19a shows the evolution of the channel conditions over time, with the throat Mach number also shown. The mass flow into the channel is initially supersonic ($M^* = 1$), but becomes subsonic at $t = 0.985$ms, as indicated by the black dotted line. The 99% rise time t_{99} is found to be 1.82ms, as indicated by the red dotted line. Figure 19b shows the propagation of the pressure wave at t_{99} through the channel length, which is estimated to take $t_p = 0.108$ms, until it reaches the transducer face at $t_r = 1.93$ms (green dotted line). In order to establish the total response time of the system, the response time of the pressure transducer must also be accounted for. This is quoted as 1ms by the manufacturer [26], giving a total response time of 2.93ms.

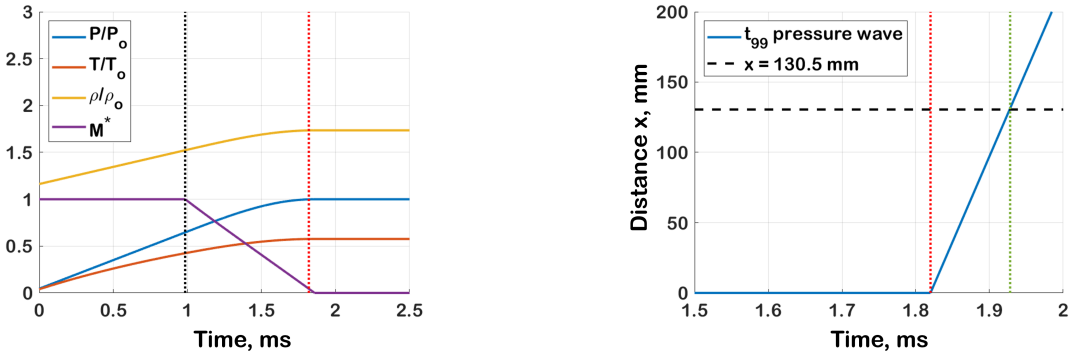

(a) Determination of t_{99}. **(b) Determination of t_r.**

Fig. 19 Response time analysis for the total pressure probe.